Front. Struct. Civ. Eng. 2020, 14(2): 280–298
https://doi.org/10.1007/s11709-019-0586-7

RESEARCH ARTICLE

Investigation of Generalized SIFs of cracks in 3D piezoelectric media under various crack-face conditions

Jaroon RUNGAMORNRAT[a], Bounsana CHANSAVANG[b], Weeraporn PHONGTINNABOOT[c*], Chung Nguyen VAN[d]

[a] *Applied Mechanics and Structures Research Unit, Department of Civil Engineering, Faculty of Engineering, Chulalongkorn University, Bangkok 10330, Thailand*

[b] *Department of Civil Engineering, Faculty of Engineering, Souphanouvong University, Loungprabang 06000, Laos*

[c] *Department of Civil Engineering, Faculty of Engineering, Burapha University, Chonburi 20131, Thailand*

[d] *Faculty of Civil Engineering, Ho Chi Minh City of Technology and Education, Ho Chi Minh 721400, Vietnam*

[*] *Corresponding author. E-mail: Weeraporn@buu.ac.th*

ABSTRACT This paper investigates the influence of crack geometry, crack-face and loading conditions, and the permittivity of a medium inside the crack gap on intensity factors of planar and non-planar cracks in linear piezoelectric media. A weakly singular boundary integral equation method together with the near-front approximation is adopted to accurately determine the intensity factors. Obtained results indicate that the non-flat crack surface, the electric field, and the permittivity of a medium inside the crack gap play a crucial role on the behavior of intensity factors. The mode-I stress intensity factors (K_{I}) for two representative non-planar cracks under different crack-face conditions are found significantly different and they possess both upper and lower bounds. In addition, K_{I} for impermeable and semi-permeable non-planar cracks treated depends strongly on the electric field whereas those of impermeable, permeable, and semi-permeable penny-shaped cracks are identical and independent of the electric field. The stress/electric intensity factors predicted by permeable and energetically consistent models are, respectively, independent of and dependent on the electric field for the penny-shaped crack and the two representative non-planar cracks. Also, the permittivity of a medium inside the crack gap strongly affects the intensity factors for all crack configurations considered except for K_{I} of the semi-permeable penny-shaped crack.

KEYWORDS crack-face conditions, intensity factors, non-flat cracks, permittivity, piezoelectric media, SGBEM

1 Introduction

Piezoelectric materials are widely employed in various engineering and industrial applications (e.g., actuators, sensors, transducers, etc.). Extensive studies have been carried out in the past decades to gain an in-depth understanding of responses and behavior of such materials in both macroscopic and microscopic scales [1–10]. Besides the desirable mechanical-electrical coupling feature, the piezoelectric materials possess a major drawback in that they are quite brittle in nature and susceptible to fracture initiation, during either the manufacturing process or usage. Therefore, extensive investigations are required to gain insights into the fracture behavior of piezoelectric materials. One of the most challenging tasks in the modeling of fractures in piezoelectric media is the development of a physically suitable mathematical model capable of simulating actual conditions on the crack surface to accurately mimic the real physical phenomena. Several models of crack-face conditions have been proposed, and their pros and cons were extensively discussed. For instance, an electrically permeable condition was introduced by Parton [11]; an electrically impermeable condition was proposed by Deeg [12]; a semi-permeable condition was employed by Hao and Shen [13]; and an energetically consistent boundary condition was proposed by Landis [14]. Among those electrical boundary conditions, an energetically consistent boundary condition seems to represent more realistic cracks than the permeable, impermeable, and semi-permeable models (an

Article history: Received Nov 16, 2018; Accepted Feb 14, 2019

extensive review can be found in the work of Rungamornrat et al. [15]). Nevertheless, most previous publications focused mainly on cracks with simple geometries (viz., Griffith cracks, straight cracks, kinked cracks/branched cracks, inclined cracks, edge cracks, and inclined edge cracks) in two-dimensional bodies and planar cracks of various shapes embedded in an infinite and/or finite three-dimensional domains under simple loading conditions [16–44], while relatively few studies relevant to the investigation of non-planar and multiple cracks have been reported, whereby most of them only concerned the development of computational tools for fracture analysis [44–49].

Selected useful results from previous investigations can be summarized as follows. For two-dimensional boundary value problems, Xu and Rajapakse [25] proposed an analytical solution for an arbitrarily oriented elliptical void embedded in a piezoelectric infinite medium. By reducing void solutions to crack solutions, they found that under varying remote electric fields and with relatively small applied remote mechanical stress, the electric intensity factors of semi-permeable and permeable cracks are nearly identical, and both results are significantly different from the solution of impermeable cracks when a crack is not parallel to the poling direction of the piezoelectric material. In contrast, when the crack is parallel to the poling direction, the electric intensity factors of impermeable and semi-permeable cracks are identical, and the solution of permeable cracks vanishes. Finally, it is interesting to note that the electric intensity factors for three types of crack-face conditions (i.e., impermeable, permeable, and semi-permeable) are nearly identical when the remote electric field is close to zero. Such finding seems valid for any orientation of the poling direction considered. Wang and Jiang [26] studied a slit crack embedded in an piezoelectric infinite medium that is subjected to far-field mechanical and electrical loadings. They found that for positive applied electric fields, the electric intensity factor of the semi-permeable crack varies from the permeable solution (the lower bound) to the impermeable solution (the upper bound) as the applied tensile stress increases. Later, Wang and Jiang [31] studied an arbitrarily oriented crack in an infinite medium subjected to mechanical and electrical loads. They found that there exists a discrepancy between the electric intensity factors computed from semi-permeable and permeable boundary conditions when the tensile mechanical load is high and the poling direction is perpendicular to the crack surfaces. This finding contradicts the results obtained by Xu and Rajapakse [25]. However, Wang and Jiang [31] pointed out that the discrepancy exists due to the different levels of applied remote mechanical load. This implies that the levels of applied mechanical and electrical loads play an important role in the fracture behavior of piezoelectric cracked media. In addition, Wang and Jiang [31] also noted that for positive applied electric fields, high mechanical loads, and when the poling direction is perpendicular to the crack surfaces, the electric intensity factor for the impermeable and permeable conditions represent the upper and lower bounds of the result for the semi-permeable condition, respectively. Conversely, if the applied electric field is negative, such solution for impermeable and permeable conditions are the lower and upper bounds of the result for the semi-permeable condition, respectively, and it can be seen that the electric intensity factor for the permeable model is independent of the electric field. Subsequently, Denda and Mansukh [46] investigated the interaction of multiple cracks in two-dimensional bodies using the boundary element method. However, their development is still limited to multiple straight cracks under impermeable and permeable boundary conditions.

For three-dimensional boundary value problems, Li and Lee [32] studied a penny-shaped crack embedded in a transversely isotropic piezoelectric infinite medium subjected to remote uniform tensile stress and constant electric field using three crack-face conditions (i.e., permeable, impermeable, and semi-permeable conditions). They found that the mode-I stress intensity factors for a penny-shaped crack under such three crack models (i.e., permeable, impermeable, and semi-permeable conditions) are identical and depend only on mechanical loading. However, the electric intensity factors for those three crack models are completely different. The electric intensity factor for semi-permeable cracks depends on various parameters (i.e., mechanical loading, electrical loading, material properties, and permittivity of the medium inside the crack gap), whereas the electric intensity factor for the impermeable condition depends only on the electrical loading. In contrast, the electric intensity factor for the permeable solution does not depend on the electrical loading but depends on the material properties and the mechanical loading. These useful conclusions are in agreement with the results obtained by several investigators [18,20,33,35].

Chiang and Weng [35] investigated a similar problem. They proposed a critical state that consists of the critical stress and applied electric displacement. They pointed out that when the effective electric displacement is positive and the remote tensile stress is less than the critical stress, the electric intensity factor for the semi-permeable model falls between the result of the impermeable model (that is the upper bound) and the result of the permeable model (that is the lower bound). However, under a positive effective electric displacement and when the remote tensile stress is greater than the critical stress, the electric intensity factor for the impermeable model becomes the lower bound whereas the results for the permeable becomes the upper bound of the results for the semi-permeable condition.

Recently, Li et al. [39] found that the mode-I stress intensity factor (as well as the electric intensity factor) for a penny-shaped crack under an energetically-consistent

boundary condition depends on various parameters besides the mechanical loading conditions (i.e., mechanical loading, electric loading, material properties, and the permittivity of the medium inside the crack gap). This finding differs from the results obtained from the impermeable, permeable, and semi-permeable boundary conditions where the mode-I stress intensity factor depends only on the mechanical loading. Moreover, as pointed out by several investigators (e.g., Li and Chen [50], Motola and Banks-Sills [51], and Li et al. [39]), the non-zero mechanical traction proposed by Landis [14] that is induced by the crack opening displacement, the jump in the electric potential, and the permittivity of the medium inside the crack gap, tends to close the crack.

As mentioned above, most previous publications focused on the modeling and analysis of planar cracks. A question arises as to the difference between the fracture behavior of planar and non-planar cracks (or curvilinear cracks and/or multiple cracks) in such materials under the four types of crack-face conditions. Recently, Rungamornrat and Mear [48] used a numerical technique called a weakly singular symmetric Galerkin boundary element method (SGBEM) to determine the stress intensity factors and electric intensity factor of an arbitrarily shaped crack embedded in three-dimensional, generally anisotropic, linear piezoelectric infinite media. They found that the fracture behavior of planar and non-planar cracks under the impermeable condition are different. More specifically, while the mechanical electrical loading can cause both stress intensity factors and electric intensity factors and vice versa factor, as observed for non-planar cracks (i.e., spherical cap cracks), there is no coupling effect due to the mechanical and electrical loads found in planar cracks (i.e., penny-shaped cracks) (e.g., [20,32,35]). Nevertheless, their investigation was restricted to impermeable cracks in infinite media.

Sanz et al. [47] and Solis et al. [49], the pioneers in the analysis of intensity factors of transversely isotropic piezoelectric finite cracked bodies, revealed that the mode-I stress intensity factor and electric intensity factor can be produced by either uniform mechanical traction or uniform electrical loading. Again, these finding are different from those in planar cracks embedded in an piezoelectric infinite domain under the impermeable assumption. However, the works of Sanz et al. [47] and Solis et al. [49] were limited to the impermeable crack-face condition only. Phongtinnaboot et al. [52] generalized the work of Rungamornrat and Mear [48] to investigate the stress intensity factors and electric intensity factor of cracked piezoelectric finite domains. The electrically impermeable assumption was still adopted for the crack surface.

Most recently, Rungamornrat et al. [15] successfully generalized the work of Rungamornrat and Mear [48] to analyze cracked piezoelectric infinite domains under the four types of electrical boundary conditions (i.e., permeable, impermeable, semi-permeable, and an energetically consistent boundary condition.) While they proposed a technique that can solve cracks of arbitrary shapes and under various electrical boundary conditions, they focused only on computational aspects and a full discussion of the role of electrical boundary conditions models was not presented. There are several crucial issues that arise and pose several nontrivial research problems in this specific area, and therefore, still require rigorous investigations, such as the difference between the fracture behavior of planar and non-planar cracks under the four types of crack-face conditions and a wide range of electrical/mechanical loads; the suitability of semi-permeable and energetically consistent conditions compared to extreme crack-face conditions such as permeable and impermeable models; the influence of the dielectric permittivity of a medium inside the crack gap, etc.

The current study is motivated by these outstanding challenges to fully explore the influence of several parameters such as crack geometry, crack-face conditions, loading conditions, and the permittivity of the medium inside the crack gap on the stress and electric intensity factors along the crack front of cracked piezoelectric bodies. Three representative configurations of cracks, including a penny-shaped crack, a spherical cap crack, and a cylindrical crack, and four models of electrical boundary conditions (viz., permeable, impermeable, semi-permeable, and an energetically consistent boundary conditions) are considered in the present study.

2 Problem description

Let us consider an isolated crack in a three-dimensional, homogeneous, linear piezoelectric, infinite medium Ω as shown in Fig. 1. The crack is represented by two identical surfaces S^+ and S^- with their corresponding outward unit normal vectors $\boldsymbol{n}^+$ and $\boldsymbol{n}^-$, respectively. The body is assumed to be free of body force and body charge, and can be subjected to mechanical and electrical loadings on either the crack surface or the remote boundary. The elastic

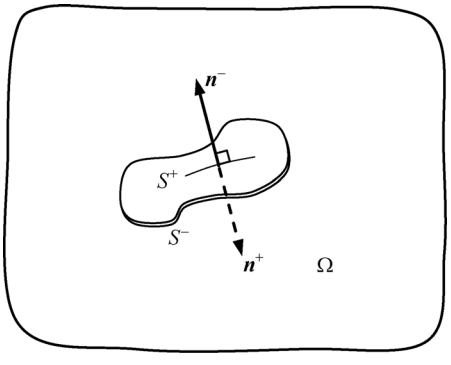

Fig. 1 Schematic of a three-dimensional, linear piezoelectric, infinite medium containing a crack.

constants, the piezoelectric constants, and the dielectric permittivities of the constituent material are fully prescribed and denoted in a concise form by E_{iJKl}. The boundary conditions on the crack surface can be simulated by one of the following four models: impermeable, permeable, semi-permeable, and energetically consistent models. The first two models ignore the contribution of the permittivity of the medium inside the crack gap, whereas such parameters is fully prescribed and its role is considered in both semi-permeable and energetically consistent models, and are assumed to be prescribed and defined by κ_c. It should be noted here that the notations and nomenclatures utilized by Rungamornrat et al. [15] are adopted in this study and detailed explanations will not be repeated here for brevity.

For impermeable cracks, the generalized tractions on the upper and lower crack surfaces, denoted by t_I^+ and t_I^-, are fully prescribed whereas the jump in the crack-face generalized displacement, defined by $\Delta u_I \equiv u_I^+ - u_I^-$, are unknown a priori. This implies that the permittivity of the medium inside the crack gap is negligible or in other words the medium between the upper and lower crack surfaces is treated as an insulator (e.g., Deeg [12]). For permeable cracks, the mechanical tractions on both crack surfaces t_i^+, t_i^-, the zero jump in the crack-face electrical potential $\Delta u_4 \equiv u_4^+ - u_4^- = 0$, and the zero sum of the crack-face electric charges $\Sigma t_4 \equiv t_4^+ + t_4^- = 0$ are fully prescribed, whereas the jump in the crack-face displacement, $\Delta u_i \equiv u_i^+ - u_i^-$ and the crack-face electric charge $t_4^+ = -t_4^-$ are unknown a priori. For this particular case, the permittivity of a medium inside the crack gap is assumed indefinitely large (e.g., Parton [11]). For semi-permeable cracks, the mechanical tractions on both crack surfaces, t_i^+, t_i^- are fully prescribed and the sum of the surface electric charges vanishes (i.e., $\Sigma t_4 = 0$) whereas the jump in the crack-face generalized displacement Δu_I and the crack-face electric charge $t_4^+ = -t_4^-$ are unknown a priori and also satisfy the following relation

$$t_4^+ \Delta u_i n_i^+ = -\kappa_c \Delta u_4, \tag{1}$$

where κ_c is the dielectric permittivity of the medium inside the crack gap (e.g., Hao and Shen [13]). It should be noted that if the permittivity inside the crack gap is significantly large (i.e., $\kappa_c \to \infty$), the electrically semi-permeable condition will converge to the conducting boundary condition (e.g., [32,35]). Here and in what follows, the lower case indices range from 1 to 3; the upper case indices range from 1 to 4, and repeated indices imply a summation over their range. Note that the superscript "+" and "−" are employed to emphasize the quantities associated with the upper crack surface S^+ and the lower crack surface S^-, respectively.

For energetically consistent cracks (e.g., Landis [14]), the mechanical tractions on both crack surfaces t_i^+, t_i^- can be partitioned into two parts: $\sigma_i^+ + \tau_i^+$ and $\sigma_i^- + \tau_i^-$ where $\{\sigma_i^+, \sigma_i^-\}$ and $\{\tau_i^+, \tau_i^-\}$ are the normal and shear tractions, respectively. For this crack model, the mechanical shear tractions $\{\tau_i^+, \tau_i^-\}$ are fully prescribed whereas the jump in the crack-face generalized displacement Δu_I, the mechanical normal tractions $\{\sigma_i^+, \sigma_i^-\}$, and the surface electric charge $t_4^+ = -t_4^-$ are unknown a priori but satisfy the condition (1) and the following relation

$$\sigma_j^+ = (1/2)\kappa_c n_j^+ (\Delta u_4)^2 / (\Delta u_i n_i^+)^2. \tag{2}$$

Extensive details of the electrical boundary conditions used in the present investigation can also be found in the work of Rungamornrat et al. [15].

3 Formulation

A set of basic equations for linear piezoelectric materials and the boundary integral equations governing an isolated crack of arbitrary shape embedded in a three-dimensional, generally anisotropic, linear piezoelectric infinite medium under various types of crack-face conditions are summarized below.

3.1 Basic field equations

The electro-mechanical behavior of a piezoelectric medium is governed by the classical theory of linear piezoelectricity. The basic field equations for a vanishing distributed source can be expressed in a concise form as

$$\frac{\partial \sigma_{iJ}}{\partial x_i} = 0, \ \sigma_{iJ} = E_{iJKl} \frac{\partial u_K}{\partial x_l}, \tag{3}$$

where σ_{iJ} represents the generalized stress (i.e., the stress tensor σ_{ij} and the electric induction vector σ_{i4}); u_K represents the generalized displacement (i.e., the displacement u_k and the electric potential u_4), and E_{iJKl} denotes the generalized moduli (i.e., elastic constants E_{ijkl}, piezoelectric constants E_{i4kl}, and dielectric permittivities $-E_{i44l}$). The generalized traction at any point on a smooth surface with a unit normal $\boldsymbol{n}$ is given by $t_J = \sigma_{iJ} n_i$ (i.e., the mechanical traction $t_j = \sigma_{ij} n_i$ and the surface electric charge $t_4 = \sigma_{i4} n_i$).

3.2 Boundary integral equations

Boundary integral equation methods have been found efficient for modeling cracks in homogenous, linear, infinite media because in the absence of a distributed source, the key governing equation involves only unknowns on the crack surface. This positive feature renders the solution methodology computationally efficient than domain-based techniques such as the conventional finite element and finite difference methods. In the

present study, the well-known, symmetric Galerkin boundary element method (SGBEM) developed by Rungamornrat and Mear [48] and Rungamornrat et al. [15] is selected as key computational procedure in the analysis.

For isolated cracks in a linear piezoelectric, infinite medium that is free of remote loading, the generalized stress σ_{lK} at any interior point $\boldsymbol{x}$ can be expressed in terms of the crack-faced data via the following standard integral relation

$$\sigma_{lK}(\boldsymbol{x}) = -\int_{S^+} S^J_{lK}(\boldsymbol{\xi}-\boldsymbol{x})\Sigma t_J(\boldsymbol{\xi})\mathrm{d}A(\boldsymbol{\xi}) + \int_{S^+} \Sigma^{lK}_{iJ}(\boldsymbol{\xi}-\boldsymbol{x})n_i(\boldsymbol{\xi})\Delta u_J(\boldsymbol{\xi})\mathrm{d}A(\boldsymbol{\xi}), \quad (4)$$

where $\Sigma t_J = t_J^+ + t_J^-$ and $\Delta u_J = u_J^+ - u_J^-$ denote the sum of the crack-face generalized traction and the jump in the crack-face generalized displacement, respectively, and $S^P_{iJ}(\boldsymbol{\xi}-\boldsymbol{x})$ and $\Sigma^{lK}_{iJ}(\boldsymbol{\xi}-\boldsymbol{x})$ are known fundamental solutions for an un-cracked whole space. While Eq. (4) can be directly used to form a boundary integral equation sufficient for determining the unknown relative crack-face generalized displacement, the resulting integral equations contain both the strongly singular kernel $S^P_{iJ}(\boldsymbol{\xi}-\boldsymbol{x})$ and the hyper-singular kernel $\Sigma^{lK}_{iJ}(\boldsymbol{\xi}-\boldsymbol{x})$ and this, as a direct consequence, requires nontrivial numerical treatments in the solution procedure (e.g., [53–57]). To avoid such difficulties, an alternative singularity-reduced boundary integral equation for the generalized crack-face traction proposed by Rungamornrat et al. [15] and Rungamornrat and Mear [48] can be utilized. To construct such weakly singular integral equation, they employed the following special decompositions of the kernels $S^P_{iJ}(\boldsymbol{\xi}-\boldsymbol{x})$ and $\Sigma^{lK}_{iJ}(\boldsymbol{\xi}-\boldsymbol{x})$:

$$S^P_{iJ}(\boldsymbol{\xi}-\boldsymbol{x}) = H^P_{iJ}(\boldsymbol{\xi}-\boldsymbol{x}) + \varepsilon_{ism}\frac{\partial G^P_{mJ}(\boldsymbol{\xi}-\boldsymbol{x})}{\partial \xi_s}, \quad (5)$$

$$\Sigma^{lK}_{iJ}(\boldsymbol{\xi}-\boldsymbol{x}) = -E_{iJKl}\delta(\boldsymbol{\xi}-\boldsymbol{x}) + \varepsilon_{ism}\frac{\partial}{\partial \xi_s}\varepsilon_{lrt}\frac{\partial}{\partial \xi_r}C^{tK}_{mJ}(\boldsymbol{\xi}-\boldsymbol{x}), \quad (6)$$

where ε_{ism} is the standard alternating symbol; $\delta(\boldsymbol{\xi}-\boldsymbol{x})$ is a Dirac-delta function centered at $\boldsymbol{x}$; $H^P_{iJ}(\boldsymbol{\xi}-\boldsymbol{x}) = -\delta_{JP}(\xi_i - x_i)/4\pi r^3$ with δ_{JP} denoting the generalized Kronecker-delta and $r = ||\boldsymbol{\xi}-\boldsymbol{x}||$; and $G^P_{mJ}(\boldsymbol{\xi}-\boldsymbol{x})$ and $C^{tK}_{mJ}(\boldsymbol{\xi}-\boldsymbol{x})$ are given, for generally anisotropic piezoelectric materials, by

$$G^P_{mJ}(\boldsymbol{\xi}-\boldsymbol{x}) = \frac{\varepsilon_{mqa}E_{qJKl}}{8\pi^2 r}\oint_{\boldsymbol{z}\cdot\boldsymbol{r}=0}(\boldsymbol{z},\boldsymbol{z})^{-1}_{KP}z_a z_l \mathrm{d}s(\boldsymbol{z}), \quad (7)$$

$$C^{tK}_{mJ}(\boldsymbol{\xi}-\boldsymbol{x}) = \frac{A^{KJPQ}_{mtsl}}{8\pi^2 r}\oint_{\boldsymbol{z}\cdot\boldsymbol{r}=0}(\boldsymbol{z},\boldsymbol{z})^{-1}_{PQ}z_s z_l \mathrm{d}s(\boldsymbol{z}),$$
$$A^{KJPQ}_{mtsl} = \varepsilon_{aum}\varepsilon_{adt}\left\{E_{uKPs}E_{dJQl} - \frac{1}{4}E_{dJKu}E_{lPQs}\right\}, \quad (8)$$

in which $\boldsymbol{z}$ is a unit vector, $(\boldsymbol{z},\boldsymbol{z})_{PQ} = z_m E_{mPQn} z_n$, $(\boldsymbol{z},\boldsymbol{z})^{-1}$ is the inverse of $(\boldsymbol{z},\boldsymbol{z})$; and the line integrals are carried out along a unit circle on the plane normal to the vector $\boldsymbol{r} = \boldsymbol{\xi}-\boldsymbol{x}$. It is remarked that the two-point functions $G^P_{mJ}(\boldsymbol{\xi}-\boldsymbol{x})$ and $C^{tK}_{mJ}(\boldsymbol{\xi}-\boldsymbol{x})$ are only singular at $\boldsymbol{\xi} = \boldsymbol{x}$ of $\mathcal{O}(1/r)$.

By applying Eqs. (5) and (6) to Eq. (4) together with carrying out the integration by parts via Stokes' theorem, it results in the singularity-reduced integral relation for the generalized stress

$$\sigma_{lK}(\boldsymbol{x}) = \varepsilon_{lrt}\frac{\partial}{\partial x_r}\int_{S^+} G^J_{tK}(\boldsymbol{\xi}-\boldsymbol{x})\Sigma t_J(\boldsymbol{\xi})\mathrm{d}A(\boldsymbol{\xi}) + \varepsilon_{lrt}\frac{\partial}{\partial x_r}\int_{S^+} C^{tK}_{mJ}(\boldsymbol{\xi}-\boldsymbol{x})D_m\Delta u_J(\boldsymbol{\xi})\mathrm{d}A(\boldsymbol{\xi}) - \int_{S^+} H^J_{lK}(\boldsymbol{\xi}-\boldsymbol{x})\Sigma t_J(\boldsymbol{\xi})\mathrm{d}A(\boldsymbol{\xi}), \quad (9)$$

Finally, a weakly singular, weak-form boundary integral equation for the generalized traction reported in Rungamornrat et al. [15] and Rungamornrat and Mear [48] can be obtained from Eq. (9) by a limiting process, a standard weighted residual technique, and the integration by parts via Stokes' theorem. Its final explicit form, in terms of the crack-face data, is given by

$$-\int_{S^+} D_t\tilde{\nu}_K(\boldsymbol{y})\int_{S^+} C^{tK}_{mJ}(\boldsymbol{\xi}-\boldsymbol{y})D_m\Delta u_J(\boldsymbol{\xi})\mathrm{d}A(\boldsymbol{\xi})\mathrm{d}A(\boldsymbol{y}) = \frac{1}{2}\int_{S^+}\tilde{\nu}_K(\boldsymbol{y})\Delta t_K(\boldsymbol{y})\mathrm{d}A(\boldsymbol{y}) + \int_{S^+} D_t\tilde{\nu}_K(\boldsymbol{y})\int_{S^+} G^J_{tK}(\boldsymbol{\xi}-\boldsymbol{y})\Sigma t_J(\boldsymbol{\xi})\mathrm{d}A(\boldsymbol{\xi})\mathrm{d}A(\boldsymbol{y}) + \int_{S^+}\tilde{\nu}_K(\boldsymbol{y})\int_{S^+} H^J_{iK}(\boldsymbol{\xi}-\boldsymbol{y})n_i(\boldsymbol{y})\Sigma t_J(\boldsymbol{\xi})\mathrm{d}A(\boldsymbol{\xi})\mathrm{d}A(\boldsymbol{y}), \quad (10)$$

where $\tilde{\nu}_K$ is a sufficiently smooth test function; $D_m(\cdot) = n_i\varepsilon_{ism}\partial(\cdot)/\partial\xi_s$ is a surface differential operator; $\Sigma t_K = t_K^+ + t_K^-$ and $\Delta t_K = t_K^+ - t_K^-$ are the sum of and the jump in the generalized tractions across the crack surface; and $\{C^{tK}_{mJ}, G^J_{tK}, n_i H^J_{iK}\}$ are known kernels. It should be noted that the development of the boundary integral equation in Eq. (10) is independent of the crack configurations and the mechanical and electrical boundary conditions on the crack surface and, as a result, it is valid for the four types of cracks described above. In addition, since it contains

complete information on the crack surface (i.e., Δt_K, Σt_K, and Δu_K), the boundary integral equation in Eq. (10) is sufficient for solving the primary unknowns on the crack surface when all prescribed data and known relations associated with each type of cracks are properly incorporated. From a theoretical and computational point of view, all the double-surface integrals in Eq. (10) exist in an ordinary sense since all involved kernels $\{C^{tK}_{mJ}, G^{J}_{tK}, n_i H^{J}_{iK}\}$ are only weakly singular and of $\mathcal{O}(1/r)$. This feature allows unknown data on the crack surface to be approximated by continuous interpolation functions. Although Eq. (10) is applicable only to an infinite domain that is free from the electro-mechanical remote loading, the integration of the remote loading can readily be handled using the principle of superposition (see clear explanations in Rungamornrat et al. [15]).

4 Solution technique

By adopting a standard discretization procedure commonly employed in the weakly singular SGBEM, the boundary integral equation for the generalized traction can be transformed into a discrete system of linear algebraic equations

$$\boldsymbol{C}\Delta\boldsymbol{U} + (\boldsymbol{G}+\boldsymbol{H})\Sigma\boldsymbol{T} + \boldsymbol{L}\Delta\boldsymbol{T} = \boldsymbol{0}, \tag{11}$$

where matrices $\boldsymbol{C}$, $\boldsymbol{G}$, and $\boldsymbol{H}$ result directly from the discretization of the double surface integrals containing the kernels C^{tK}_{mJ}, G^{J}_{tK}, and H^{J}_{iK}, respectively; the matrix $\boldsymbol{L}$ corresponds to a single surface integral containing the jump in the crack-face generalized traction; $\Delta\boldsymbol{U}$ is a vector of nodal quantities associated with the jump in the crack-face generalized displacement, and $\Sigma\boldsymbol{T}$ and $\Delta\boldsymbol{T}$ are vectors of nodal quantities of the sum of and the jump in the crack-face generalized tractions, respectively. The construction of all matrices $\{\boldsymbol{C}, \boldsymbol{G}, \boldsymbol{H}, \boldsymbol{L}\}$ follows directly the work of [15,48]. The approximation of the near-front, jump in the crack-face generalized displacement is enhanced by using special crack-tip elements along the crack front [15,48,58] and the interpolation technique is employed to efficiently evaluate involved kernels for general anisotropic materials [15,48]. In addition to allowing the use of relatively coarse meshes in the discretization while yielding sufficiently accurate results, the former also provides the direct means to extract the intensity factors in terms of extra nodal data solved along the crack front. Details of such relevant solution procedure can be found in the work of Rungamornrat and Mear [48] and Rungamornrat et al. [15].

To obtain the unknown crack-face data, the system of linear Eq. (11) is solved together with the prescribed crack-face boundary conditions. For both electrically permeable and impermeable cracks, the final system of governing equations after incorporating the crack-face conditions is linear and its solution can be readily obtained via a selected efficient linear solver. On the contrary, the final governing equations for the case of electrically semi-permeable and energetically consistent cracks are nonlinear due to the nonlinear crack-face conditions and they are efficiently solved via standard Newton iterative scheme. Details of the solution procedure can be found in the work of Rungamornrat et al. [15]. Once a set of nodal data $\Delta\boldsymbol{U}$ is determined, it is directly used to post-process for both the stress and electric intensity factors along the crack front.

5 Numerical results and discussions

First, computed results for certain simple cases such as a penny-shaped crack under simple electrical/mechanical loads are benchmarked with available reference solutions to validate the formulation of the governing integral equations and numerical implementations of the weakly singular SGBEM and the post-process for the stress intensity factors and the electric intensity factor. After verifying the proposed technique, we then thoroughly investigated the influence of non-flat geometry of the crack surface, remote electrical load, and permittivity of the medium inside the crack gap on the intensity factors along the crack front of representative non-flat cracks.

In the numerical study, a series of meshes is constructed first to investigate the convergence of the computed intensity factors and a sufficiently fine mesh is then chosen to ensure the convergence of the solution. In the discretization, the majority of the crack surface is discretized by standard 6-node and 8-node isoparametric elements, whereas the region adjacent to the crack boundary is discretized by 9-node special crack-tip elements [15,48,58]. The representative linear piezoelectric materials selected in the analysis are transversely isotropic and all material constants are taken to be those of PZT-4, as shown in Table 1.

5.1 Verification

To verify the implemented weakly singular SGBEM,

Table 1 Generalized moduli of PZT-4 [39]. The plan of isotropy is taken normal to the x_3 -axis

item	elastic constants ($\times 10^9$ Pa)					piezoelectric constants (C/m^2)			dielectric permittivities ($\times 10^{-9}$ C/(Vm))	
	E_{1111}	E_{1122}	E_{1133}	E_{3333}	E_{1313}	E_{1143}	E_{3343}	E_{1341}	$-E_{1441}$	$-E_{3443}$
value	139.00	77.80	74.30	113.00	25.60	−6.98	13.80	13.40	6.00	5.47

consider first a penny-shaped crack of radius a embedded in a piezoelectric infinite medium made of PZT-4, as shown in Fig. 2(a). The medium is loaded by a uniform remote tension σ_0 that is varied from 10 to 100 MPa, whereas the electric field E_0 is fixed at 2.5 MV/m, and the dielectric permittivity of the medium inside the crack gap is chosen as $\kappa_c = 5\kappa_0$ where $\kappa_0 = 8.85 \times 10^{-12}$ C/(Vm) is the permittivity of the air. The poling direction and the axis of material symmetry are taken along the x_3 -axis. The mesh shown in Fig. 2(b), after the convergence is confirmed, is used in the verification. Numerical results for the normalized mode-I stress intensity factor and electric intensity factor are reported in Figs. 3(a) and 3(b), respectively, along with the analytical solutions [32,39].

It is shown that the numerical results obtained are in good agreement with the analytical solution for all four crack-face condition considered. In addition, it can be inferred from Fig. 3(a) that the mode-I stress intensity factors K_I for the permeable, impermeable, and semi-permeable crack models are identical for the entire range of the applied uniform remote tension σ_0 treated. These findings are in agreement with the work of previous investigators (e.g., Li and Lee [32] and Chiang and Weng [35]) who pointed out that the mode-I stress intensity factors for the three crack-face conditions depend only on the mechanical loading but are independent of electrical loading and the permittivity of the medium inside the crack gap.

In addition, it can be concluded from Fig. 3(a) that the results predicted by the energetically consistent model is less than those predicted by the other three crack models for the entire range of σ_0. This is because, as pointed out by several investigators [50,51], the unknown mechanical traction acting on both the crack surfaces that is induced by the opening displacement of the crack, the jump in the electric potential, and the permittivity of the medium inside the crack gap, try to close the crack. However, when the uniform remote tension increases, the mode-I stress intensity factor predicted by the energetically consistent model tends to approach the results of the other three crack models.

In contrast to K_I, the electric intensity factor K_{IV} strongly depends on the electrical boundary conditions adopted on the crack surface. Results in Fig. 3(b) show that the electric intensity factors of the impermeable and permeable cracks serve, respectively, as the upper and lower bounds of the results generated by the semi-permeable and energetically consistent models for almost the entire range of σ_0 considered. However, when the uniform remote tension σ_0 is relatively small, the electric intensity factor K_{IV} for

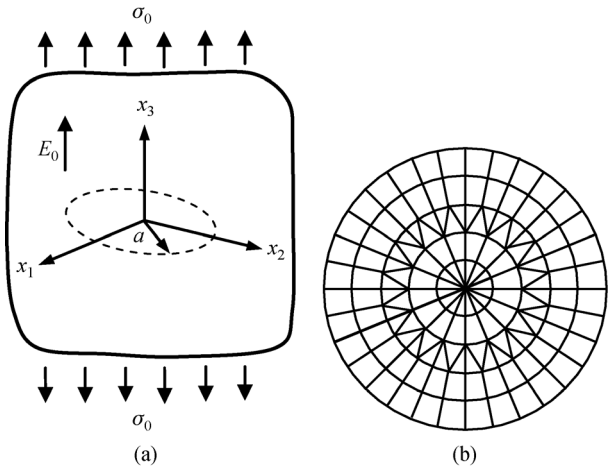

Fig. 2 (a) Schematic of a penny-shaped crack of radius a in a piezoelectric infinite medium and (b) mesh of a penny-shaped crack used in the analysis.

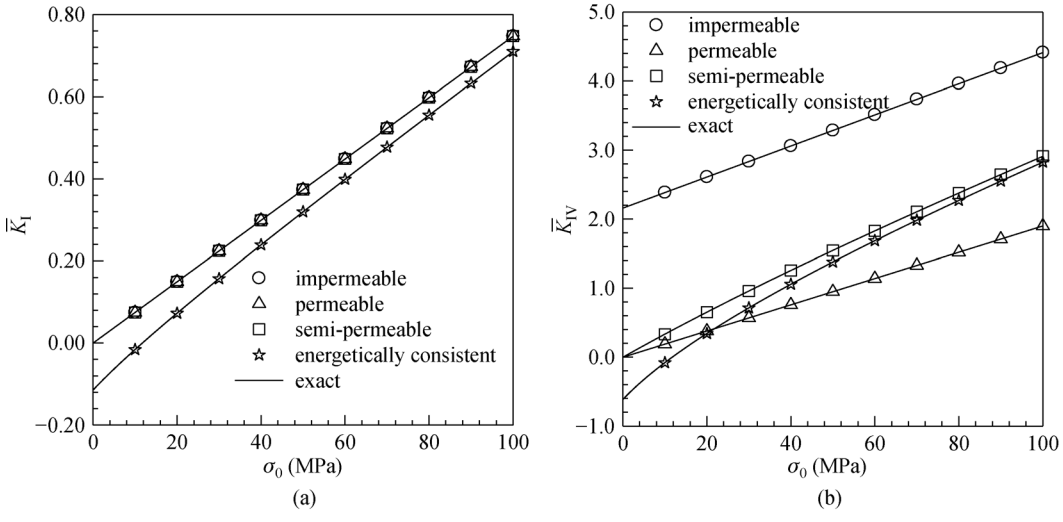

Fig. 3 Normalized intensity factors for a penny-shaped crack in a piezoelectric infinite medium subjected to remote uniform tensile stress σ_0 and constant electric field E_0 under four types of crack assumptions: (a) $\overline{K}_I = (K_I E_{3343})/(E_{1111}E_{1441}E_0\sqrt{a})$; (b) $\overline{K}_{IV} = K_{IV}/(E_{1441}E_0\sqrt{a})$.

the energetically consistent model is lower than that for the permeable model. This implies that the level of applied mechanical load has a significant influence on the lower bound of K_{IV} for the penny-shaped crack subjected to uniform loading. As a result, one can see that the lower bound of K_{IV} switches from the energetically consistent solution to the permeable solution as the applied mechanical loading increases. It is remarked also that the electric intensity factor K_{IV} for the semi-permeable and energetically consistent cracks are nearly identical and both results tend to approach the result for the impermeable model when the applied remote stress increases.

5.2 Influence of crack geometry

To explore the behavior of the intensity factors along the boundary of non-flat cracks, two representative cracks, one for a spherical cap crack (shown in Fig. 4) and the other for a cylindrical crack (shown in Fig. 5), are considered. The latter and the former are chosen to represent cracks possessing the curvature in a single direction and two directions, respectively. In the numerical study, following parameters are employed: (i) various half-subtended angles of the spherical cap crack and the cylindrical crack (defined further below in Sections 5.2.1 and 5.2.2) ranging from 5° to 90° are considered; (ii) the uniform remote tension and the uniform electric field are taken as 50 MPa and 2.5 MV/m, respectively; (iii) the permittivity of the medium inside the crack gap for both semi-permeable and energetically consistent crack-face conditions are taken as $\kappa_c = 5\kappa_0$ where $\kappa_0 = 8.85 \times 10^{-12}$ C/(Vm).

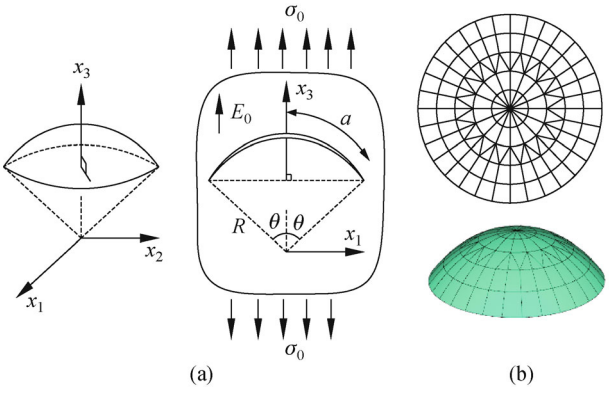

Fig. 4 (a) Schematic of a penny-shaped crack folded in circular ball (a spherical cap crack) in an infinite piezoelectric medium and (b) mesh of a spherical cap crack adopted in the analysis.

5.2.1 Spherical cap crack

Consider a spherical cap crack embedded in a transversely isotropic piezoelectric infinite medium of PZT-4, as shown schematically in Fig. 4(a). The medium is subjected to a uniform remote tension σ_0 and a uniform electric field E_0 along the x_3 -axis. The axis of material symmetry and the poling direction are chosen to direct along the x_3 -axis. The geometry of the crack surface is defined by

$$x_1 = R\sin\gamma\cos\beta,\ \ x_2 = R\sin\gamma\sin\beta,\ \ x_3 = R\cos\gamma, \quad (12)$$

where R denotes the radius of the spherical cap crack, $\beta \in [0,2\pi]$, and $\gamma \in [0,\theta]$ with θ denoting the half subtended angle of the spherical surface. It is remarked that the spherical cap crack considered here can be viewed as a penny-shaped crack of radius $a = R\theta$ bended over the surface of a sphere of radius R. In the following investigation, a mesh of the crack surface containing 144 elements is adopted, as shown in Fig. 4(b).

The normalized non-zero stress intensity factors K_{I} and K_{II}, and the electric intensity factor K_{IV} under the four crack-face conditions are shown in Figs. 6(a)–6(c), respectively. It is found that when the half subtended angle of the crack surface is relatively small, the behavior of the intensity factors of the spherical cap crack is similar to that of the penny-shaped crack. However, when the half subtended angle is sufficiently large, such behavior of the special cap crack is significantly different from that of the penny-shaped crack.

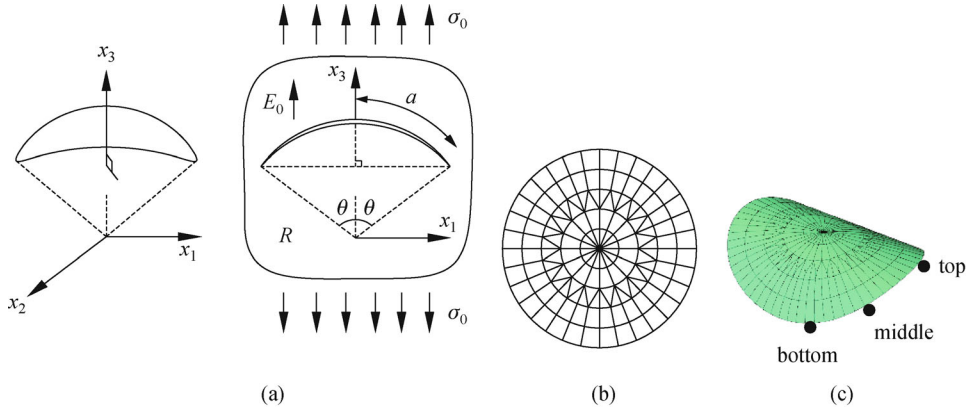

Fig. 5 (a) Schematic of a penny-shaped crack folded over the surface of a sphere of radius R (a cylindrical crack) in a piezoelectric infinite medium; (b) mesh utilized in the analysis; (c) three different points on the mesh of cylindrical crack observed in the investigation.

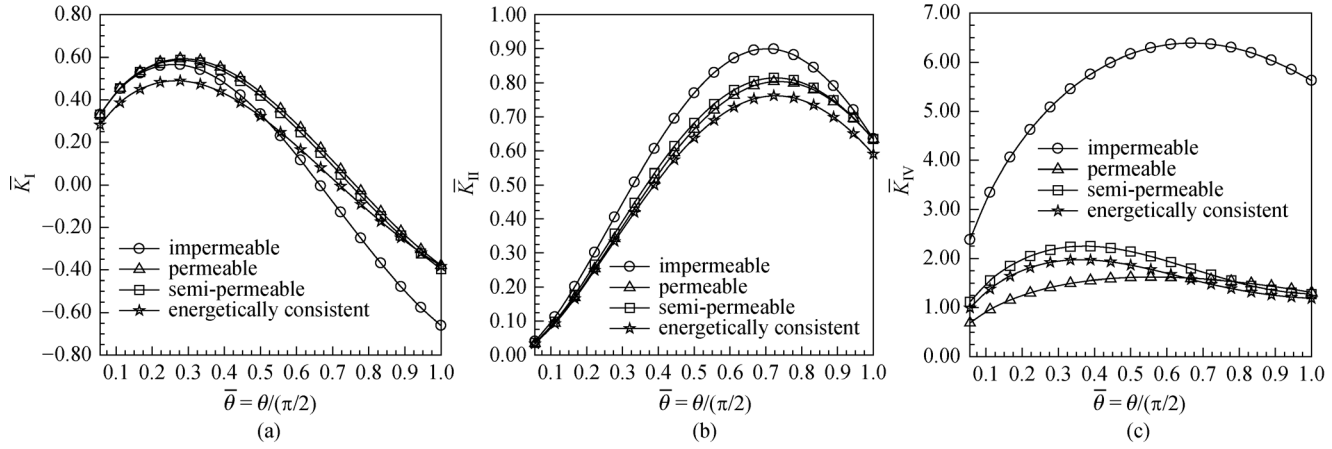

Fig. 6 Dependence of the normalized intensity factors on half-subtended angles for the spherical cap crack in a piezoelectric infinite medium: (a) $\overline{K}_{\mathrm{I}} = K_{\mathrm{I}}/(\sigma_0\sqrt{R})$; (b) $\overline{K}_{\mathrm{II}} = K_{\mathrm{II}}/(\sigma_0\sqrt{R})$; (c) $\overline{K}_{\mathrm{IV}} = (K_{\mathrm{IV}}E_{3333})/(\sigma_0 E_{3343}\sqrt{R})$.

The results reported in Fig. 6(a) indicate that when the half subtended angle of the crack surface is relatively small (e.g., $\theta = 5°,\ 10°,\ 15°$), the distribution of K_{I} under the four crack models is similar to that of K_{I} for the penny-shaped crack. In particular, K_{I} of the impermeable, permeable, and semi-permeable cracks are nearly identical and serve as the upper bound, whereas K_{I} of the energetically consistent model is less than those of the other three crack models and, therefore, serves as the lower bound solution. However, when the half subtended angle is sufficiently large, the distributions of K_{I} for the impermeable, permeable, and semi-permeable crack models are obviously different and the solution predicted by the permeable model forms the upper bound, whereas K_{I} for the impermeable model becomes the lower bound instead of the result generated by the energetically consistent model. It can be concluded that the lower bound switches from the energetically consistent solution to the impermeable solution as the half subtended angle increases.

It is important to remark that while the mode-I stress intensity factors of the penny-shaped crack under the impermeable, permeable, and semi-permeable crack-face conditions are identical as indicated in Refs. [32,39], such results for the spherical cap crack are not identical when the half subtended angle is sufficiently large. The discrepancy depends primarily on the half subtended angle. This implies that the non-planar feature of the crack surface has a significant influence on the mode-I stress intensity factor of the three crack models. According to the numerical results presented later in Section 5.3, it was also found that the non-flat crack surface leads to the dependence of the mode-I stress intensity factor K_{I} on the electric field for both the impermeable and semi-permeable models, while the electric field has no effect on K_{I} of the penny-shaped crack under the impermeable, permeable, and semi-permeable crack-face conditions. This conclusion is supported by the significant difference among results generated by the three crack models (i.e., impermeable, permeable, and semi-permeable models) when the half subtended angle of the spherical cap crack is sufficiently large.

While the lower bound of the mode-I stress intensity factor for the spherical cap crack switches when the half subtended angle is sufficiently large, the upper and lower bounds of the mode-II stress intensity factor for the spherical cap crack do not. Results in Fig. 6(b) indicates that the mode-II stress intensity factor K_{II} for the impermeable and energetically consistent cracks serve, respectively, as the upper and lower bounds for (nearly) the entire range of the normalized half subtended angle $\overline{\theta}$, except when θ is either very small or large (i.e., $\theta = 5°$ and $\theta = 90°$). In particular, the numerical result indicates that when the half-subtended angle is relatively small (e.g., $\theta = 5°$), results generated by the four crack-face models are nearly identical and almost zero. This finding is similar to that for the penny-shaped crack subjected to uniform remote loading where the mode-II stress intensity factors for the four crack-face models vanish. However, such result becomes clearly distinct when the half subtended angles become larger (e.g., $\theta = 40°,\ 45°,\ 50°,\ 55°$) for the four crack-face models, and it can be seen that the impermeable solution is significantly different from those of the other three crack-face models. Finally, it should be noted that when the half subtended angle is relatively large (i.e., $\theta = 90°$), the mode-II stress intensity factor K_{II} for the impermeable, permeable, and semi-permeable cracks are nearly identical.

Similar to the mode-I stress intensity factor but unlike the mode-II stress intensity factor, the lower bound of the electric intensity factor K_{IV} for the spherical cap crack switches as the half subtended angle increases. Results in Fig. 6(c) indicate that the electric intensity factors K_{IV} for the four crack-face models are different, and that the permeable solution represents the lower bound when the

half subtended angle is relatively small. However, when the half subtended angle becomes larger (e.g., $\theta = 65°$, 70°), the energetically consistent solution becomes the lower bound instead for the permeable solution. Moreover, it is obvious that when the half subtended angle of the spherical cap crack is relatively small, K_{IV} of the spherical cap crack for the four crack-face models possesses a similar behavior to that of the penny-shaped crack, where the permeable solution of K_{IV} serves as the lower bound. However, K_{IV} of the spherical cap crack and the penny-shaped crack obviously exhibit different behavior when the half subtended angle is sufficiently large, and it can be seen that the lower bound switches from the permeable solution to the energetically consistent solution. Finally, it can be inferred from Figs. 3(b) and 6(c) that K_{IV} for the impermeable model is still the upper bound for both the penny-shaped crack and the spherical cap crack for the entire range of the half subtended angle θ considered.

5.2.2 Cylindrical crack

Consider a cylindrical crack with the radius of curvature R embedded in a transversely isotropic piezoelectric infinite medium made of PZT-4, as illustrated in Fig. 5(a). The piezoelectric medium is subjected to a uniform remote tension σ_0 and a uniform electric field E_0 along the x_3 -axis. The axis of the material symmetry and the poling direction coincide with the x_3 -axis.

The geometry of the crack surface is defined by

$$x_1 = R\sin\gamma, \quad x_2 \in [-d,d], \quad x_3 = R\cos\gamma, \tag{13}$$

where $\gamma \in [0,\theta]$, θ denotes the half subtended angle of the crack surface, and $d = R\sqrt{\theta^2 - \gamma^2}$. It is worth noting that the cylindrical crack considered here can be obtained directly by folding a penny-shaped crack of radius $a = R\theta$ over the surface of a cylinder of radius R. In the present study, a mesh of the cylindrical crack containing 144

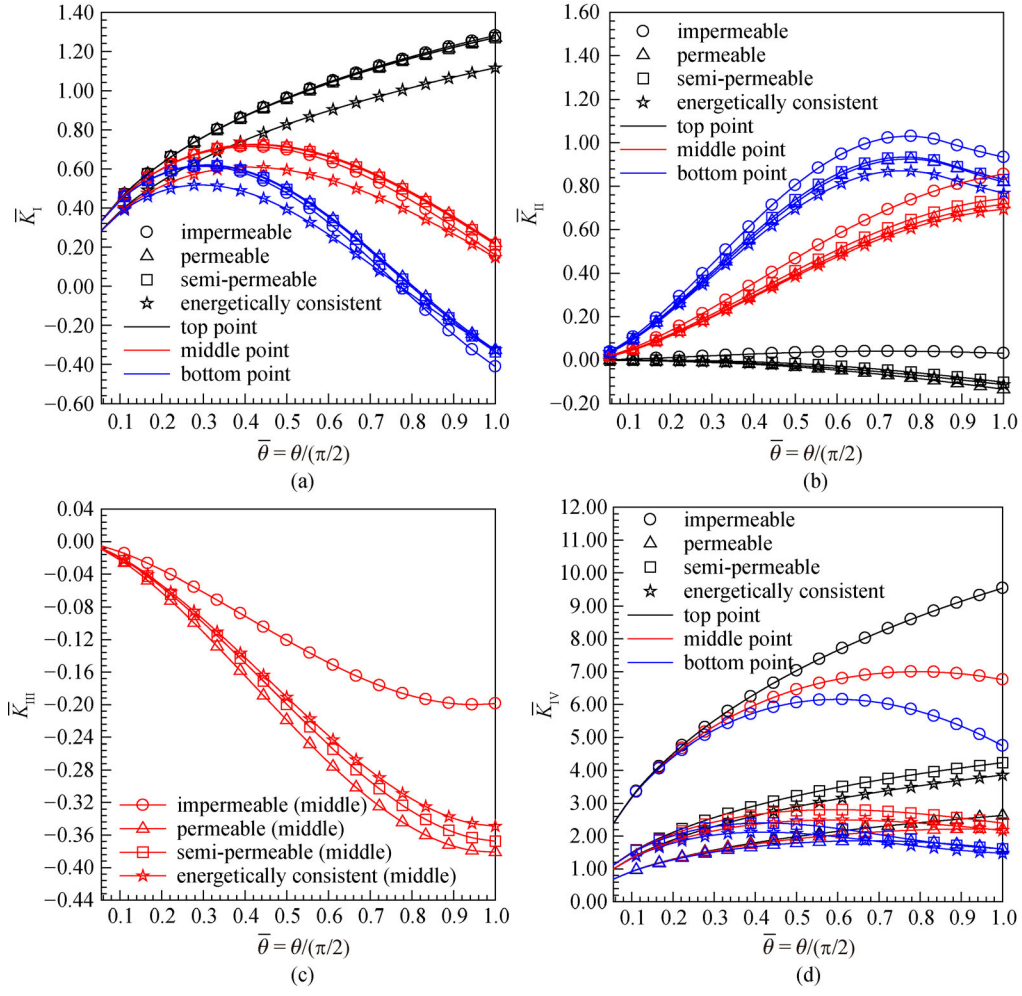

Fig. 7 Dependence of the normalized intensity factors on the half-subtended angles for a cylindrical crack in a piezoelectric infinite medium: (a) $\overline{K}_{\mathrm{I}} = K_{\mathrm{I}}/(\sigma_0\sqrt{R})$; (b) $\overline{K}_{\mathrm{II}} = K_{\mathrm{II}}/(\sigma_0\sqrt{R})$; (c) $\overline{K}_{\mathrm{III}} = K_{\mathrm{III}}/(\sigma_0\sqrt{R})$; (d) $\overline{K}_{\mathrm{IV}} = (K_{\mathrm{IV}}E_{3333})/(\sigma_0 E_{3343}\sqrt{R})$.

elements is used, as shown in Fig. 5(b). The normalized stress intensity factors $\{K_{\mathrm{I}},K_{\mathrm{II}},K_{\mathrm{III}}\}$ and the electric intensity factor K_{IV} at three different points (i.e., top, middle, and bottom points) located on the cylindrical crack as shown in Fig. 5(c) are reported in Figs. 7(a)–7(d) for four crack-face models.

Results in Fig. 7(a) indicate that the mode-I stress intensity factor K_{I} for the top point is greater than those for the middle and bottom points of the cylindrical crack, when the half-subtended angle is relatively large. Moreover, it can be inferred from Fig. 7(a) that K_{I} under the four types of crack-face conditions obtained from the top and bottom points of the cylindrical crack are similar to the results for the penny-shaped crack and spherical cap crack, respectively, whereas such intensity factors obtained for the middle point are different from those for the penny-shaped crack and the spherical cap crack. In particular, it was found that for the top point, K_{I} for the impermeable, permeable, and semi-permeable cracks are nearly identical, whereas that for the energetically consistent model is less than those for the other three crack-face models and, therefore, serves as the lower bound for the entire range of the normalized half-subtended angle $\overline{\theta}$. While K_{I} at the top point of the cylindrical crack obtained from the four crack models are similar to that of the penny-shaped crack, the results at the bottom point has the similar behavior to that of the spherical cap crack. It was also found that K_{I} at the bottom point of the cylindrical crack obtained from the impermeable, permeable and semi-permeable models are not identical, and that the permeable solution serves as the upper bound, whereas the lower bound of K_{I} switches from the energetically consistent model to the impermeable model when the subtended angle of the cylindrical crack increases. In contrast to the top and bottom points of the cylindrical crack, K_{I} at the middle point under the four crack-face conditions are different from the results obtained for the penny-shaped crack and the spherical cap crack. In particular, it can be seen that results for the impermeable, permeable, and semi-permeable crack-face models are not nearly identical as those observed at the top point and that the permeable solution serves as the upper bound, whereas the energetically consistent solution represents the lower bound for the entire range of the normalized half-subtended angle $\overline{\theta}$.

While the mode-II stress intensity factor K_{II} for the penny-shaped crack subjected to uniform loading identically vanishes along the crack front, it is nonzero and completely different for the top, middle, and bottom points of the cylindrical crack. Results in Fig. 7(b) indicate that K_{II} obtained at the bottom point is greater than those at the middle and top points of the cylindrical crack. In addition, it is obvious that when the half-subtended angle is relatively small (e.g., $\theta = 5°$), the mode-II stress intensity factors at all three points of the cylindrical crack for all four crack-face models are nearly identical and almost vanish. However, when the half-subtended angle increases, the stress intensity factors K_{II} for the four crack-face models are different and their lower and upper bounds can be obviously seen. More specifically, it can be inferred from Fig. 7(b) that when the half-subtended angle is sufficiently large, the impermeable crack model yields the upper bound for K_{II} at all three points of the cylindrical crack, whereas the permeable and energetically consistent crack models provide the lower bound of K_{II} at the top point and the remaining two points (i.e., middle and bottom points), respectively. This indicates that the non-planar feature of the crack surface has the significant influence on the lower bound and the value of the mode-II stress intensity factor for the cylindrical crack. As a result, it can be seen that K_{II} obtained from the four crack models are different and that the upper and lower bounds exist when the half-subtended angle becomes larger. In addition, the lower bounds of K_{II} are not the same for the top point and the remaining two points of the cylindrical crack. Finally, it can be observed that when the half-subtended angle of the cylindrical crack is sufficiently large, K_{II} at the top point of the cylindrical crack obtained from the impermeable model is positive and quite different from those obtained from the other three models which clearly attain the negative values.

While the mode-III stress intensity factors K_{III} at the top and bottom points of the cylindrical crack for the four crack-face conditions vanish due to the symmetry, it does not vanish at the middle point of the cylindrical crack and possesses the same negative sign. Results in Fig. 7(c) also indicate that K_{III} obtained from the semi-permeable and energetically consistent crack-face models fall between the impermeable and permeable solutions which constitute the upper and lower bounds, respectively. Moreover, it was also observed that when the half-subtended angle is relatively small (i.e., $\theta = 5°$), K_{III} for the four crack-face conditions tends to zero. This finding is expected since the mode-III stress intensity factor vanishes for any planar cracks (e.g., penny-shaped cracks) subjected to uniform loading. Finally, it can be pointed out that, similar to the mode-II stress intensity factor K_{II}, K_{III} for the impermeable model is significantly different from those generated by the other three crack-face models when the half-subtended angle becomes larger.

The electric intensity factor K_{IV} at the top, middle, and bottom points of the cylindrical crack are shown in Fig. 7(d). It was found that K_{IV} at the top point is greater than those at the middle and bottom points. Moreover, obtained numerical results also indicate that the behavior of K_{IV} at the top and bottom points of the cylindrical crack is similar to that for the penny-shaped crack and the spherical cap crack, respectively, whereas K_{IV} at the middle point is significantly different from that of the penny-shaped and spherical cap cracks. More specifically, it was found that at the top point of the cylindrical crack, the electric intensity factor K_{IV} for the four crack models

are completely different according to the electrical boundary conditions adopted on the crack surface. It can be seen that the impermeable and permeable crack models yield, respectively, the upper and lower bounds of K_{IV} to the solutions from the semi-permeable and energetically consistent models. This finding is similar to the results obtained for the penny-shaped crack. Obtained results also indicate that the electric intensity factor K_{IV} at the bottom point of the cylindrical crack obtained from the four crack models is different from that of the penny-shaped crack, but is similar to that of the spherical cap crack. In addition, the impermeable crack model yields the upper bound for K_{IV} for the entire range of the normalized half-subtended angle $\overline{\theta}$, whereas the lower bound fluctuates between solutions generated by the permeable and energetically consistent crack models as $\overline{\theta}$ increases. Finally, it can be seen that when the half-subtended angle is large (e.g., $\theta = 75°, 80°, 85°, 90°$), the electric intensity factor K_{IV} of the permeable crack is nearly identical to that of the semi-permeable crack. In contrast to the top and bottom points, K_{IV} obtained at the middle point of the cylindrical crack is different from those of the penny-shaped and spherical cap cracks. It was found that the permeable crack provides the lower bound solution for K_{IV} for almost the entire range of the normalized half-subtended angle $\overline{\theta}$ except when the subtended angle is significantly large (e.g., $\theta = 85°, 90°$). Solutions generated by the permeable and energetically consistent crack models are nearly identical and serve as the lower bound. It is interesting to note that though the lower bound of K_{IV} for all three points of the cylindrical crack are completely different; the impermeable crack model always yields the upper bound of K_{IV} for all those three points.

5.3 Influence of remote electrical loading

To explore the influence of remote electrical loading on the intensity factors along the crack front of non-flat cracks, the same spherical cap crack and cylindrical crack embedded in a transversely isotropic piezoelectric infinite medium made of PZT-4 as shown in Figs. 4 and 5, respectively, are considered. In the numerical study, following parameters are employed: (i) the half-subtended angle for both cracks is taken as $\theta = 45°$; (ii) the uniform remote tension σ_0 is taken to be 50 MPa whereas the uniform electric field E_0 varies from −4.5 to 4.5 MV/m; (iii) the permeable, impermeable, semi-permeable, and energetically consistent crack models are considered; (iv) the permittivity of the medium inside the crack gap for both semi-permeable and energetically consistent crack models are taken to be $\kappa_{\mathrm{c}} = 5\kappa_0$ where $\kappa_0 = 8.85\times 10^{-12}$ C/(Vm). In the analysis of the spherical cap crack and cylindrical crack, the meshes shown in Figs. 4(b) and 5(b) are employed, respectively. In addition, results for a penny-shaped crack of radius $a = R\theta$ are also obtained and used in the comparison and discussion.

5.3.1 Spherical cap crack

The normalized non-zero stress intensity factors K_{I}, K_{II}, and the electric intensity factor K_{IV} under four types of crack-face conditions are shown in Figs. 8(a)–8(c), respectively. It can be seen from the results reported in Fig. 8(a) that the mode-I stress intensity factor K_{I} for the impermeable and semi-permeable spherical cap cracks depends strongly on the electric field E_0. These findings are in contrast with those observed for planar cracks (i.e., a penny-shaped crack) where K_{I} for impermeable, permeable, and semi-permeable cracks are identical and independent of the electric field. Moreover, it was also observed that K_{I} for permeable planar and non-planar cracks are independent of the electric field. This implies that the curvature of non-planar cracks leads to the dependence on the electric field for K_{I} for both the

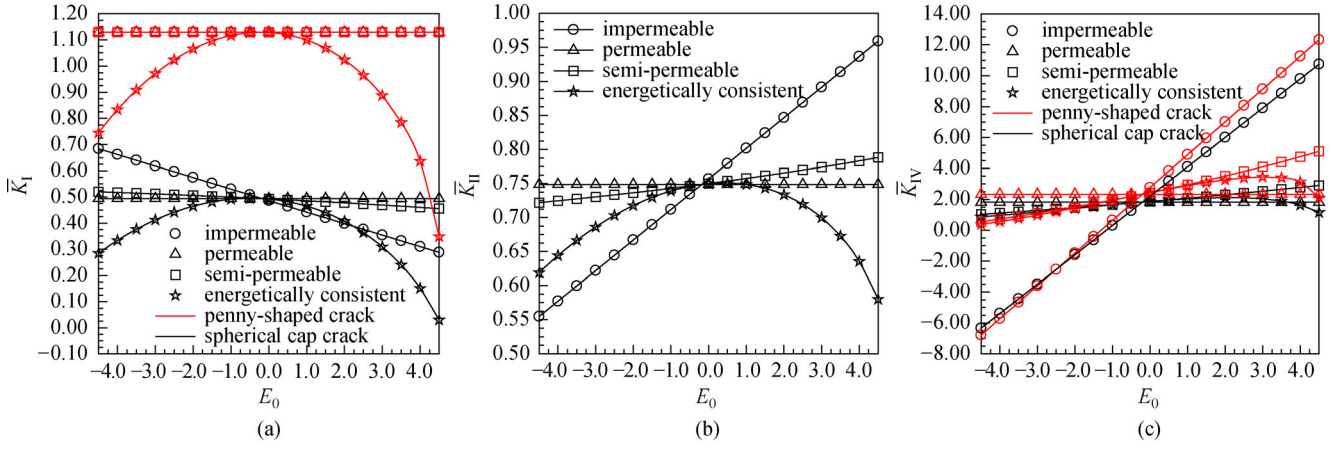

Fig. 8 Dependence of the normalized intensity factors on the electric field for a spherical cap crack in a piezoelectric infinite medium: (a) $\overline{K}_{\mathrm{I}} = K_{\mathrm{I}}/(\sigma_0\sqrt{a})$; (b) $\overline{K}_{\mathrm{II}} = K_{\mathrm{II}}/(\sigma_0\sqrt{a})$; (c) $\overline{K}_{\mathrm{IV}} = (K_{\mathrm{IV}}E_{3333})/(\sigma_0 E_{3343}\sqrt{a})$.

impermeable and semi-permeable crack-face conditions. However, such effect plays no role on the value of K_I for the permeable condition. Moreover, it can be inferred from Fig. 8(a) that the mode-I stress intensity factor generated from the energetically consistent model strongly depends on the electric field for both the penny-shaped crack and the spherical cap crack. In addition, obtained numerical results also indicate that the energetically consistent crack-face model yields the lower bound of K_I for the penny-shaped crack subjected to the uniform loading for the entire range of the electric field considered, while the lower bound of the spherical cap crack for the positive electric field fluctuates between the impermeable and energetically consistent solutions by showing a turning point at about $E_0 = 2.5$ MV/m. Moreover, it was also observed that K_I for all four crack-face conditions are nearly identical when the electric field vanishes, i.e., $E_0 = 0$ MV/m. This finding is equally true for both the penny-shaped and spherical cap cracks, as shown in Fig. 8(a). Similar to the mode-I stress intensity factor, Fig. 8(b) indicates that the mode-II stress intensity factor K_{II} for the permeable spherical cap crack is independent of the electric field, whereas K_{II} of the impermeable, semi-permeable, and energetically consistent spherical cap cracks depend strongly on the electric field.

While the fracture behavior of planar cracks (i.e., penny-shaped cracks) and non-planar cracks (i.e., spherical cap cracks) are different for the mode-I stress intensity factor when using the impermeable and semi-permeable conditions, Fig. 8(c) indicates that the electric intensity factor K_{IV} for the spherical cap crack is similar to K_{IV} of the penny-shaped crack under all four crack-face conditions. More specifically, K_{IV} is independent of the electric field for both the permeable penny-shaped and spherical cap cracks, whereas K_{IV} for the impermeable, semi-permeable, and energetically consistent crack-face models depend strongly on the electric field for both crack configurations.

According to the numerical results for the penny-shaped and spherical cap cracks subjected to remote uniform loading, the non-zero intensity factors $\{K_I,K_{II},K_{IV}\}$ for the spherical cap crack and the non-zero intensity factors $\{K_I,K_{IV}\}$ for the penny-shaped crack are all independent of the electric field under the permeable condition.

5.3.2 Cylindrical crack

The normalized stress intensity factors K_I, K_{II}, and K_{III} and the electric intensity factor K_{IV} under four types of crack-face conditions are shown in Figs. 9(a)–9(d), respectively. It can be seen from the results reported in Fig. 9(a) that the mode-I stress intensity factor K_I at the top point is greater than those at the middle and bottom points of the cylindrical crack. Moreover, it can be inferred from Fig. 9(a) that K_I at the top point of the impermeable, permeable, and semi-permeable cracks are nearly identical, whereas that of the energetically consistent crack strongly depends on the electric field. These findings are similar to the case of the penny-shaped crack subjected to uniform loading as shown in Fig. 8(a). In contrast, the behavior of K_I obtained from the three crack models for the remaining two points (i.e., middle and the bottom points) of the cylindrical crack is different from that of the penny-shaped crack but similar to that of the spherical cap crack. Figure 9(a) indicates that the impermeable, permeable, and semi-permeable models yield slightly different K_I at the middle point but clearly different at the bottom point of the cylindrical crack. In addition, it can be seen that K_I for the impermeable and semi-permeable cases depend on the electric field whereas K_I for the permeable case is independent of the electric field. Finally, it should be noted that K_I generated from the energetically consistent model strongly depends on the electric field for all three points of the cylindrical crack, similar to that of the penny-shaped crack.

While the mode-II stress intensity factor K_{II} vanishes identically for the penny-shaped crack subjected to uniform loading, it is non-zero for the top, middle, and bottom points of the cylindrical crack. Figure 9(b) indicates that K_{II} at the bottom point is greater than those at the middle and top points. Moreover, it can be inferred from Fig. 9(b) that K_{II} for the impermeable, semi-permeable, and energetically consistent models depend on the electric field and vary according to the electrical boundary condition adopted on the crack surface (except when the electric field is equal to zero where K_{II} for the four crack models are nearly identical), whereas K_{II} for the permeable model is independent of the electric field. These findings are similar for all three points of the cylindrical crack, as shown in Fig. 9(b). While the mode-III stress intensity factor K_{III} at the top and bottom points of the cylindrical crack vanish, Fig. 9(c) shows that it does not vanish at the middle point. It was observed that, similar to the mode-II stress intensity factor, K_{III} at the middle point of the cylindrical crack for the impermeable, semi-permeable, and energetically consistent models depend on the electric field, whereas that for the permeable model is clearly independent of the electric field.

The electric intensity factor K_{IV} obtained at the top, middle, and bottom points of the cylindrical crack are shown in Fig. 9(d). It was observed that, for the positive electric field, K_{IV} at the top point is greater than those at the middle and bottom points. Moreover, it was found that the behavior of K_{IV} at all three points of the cylindrical crack is similar to that of the spherical cap crack and the penny-shaped crack. More specifically, the numerical results indicate that K_{IV} for the impermeable, semi-permeable, and energetically consistent models depend strongly on the electric field, whereas K_{IV} at all three points of the cylindrical crack for the permeable model is independent of the electric field.

Finally, it is important to note that the intensity factors

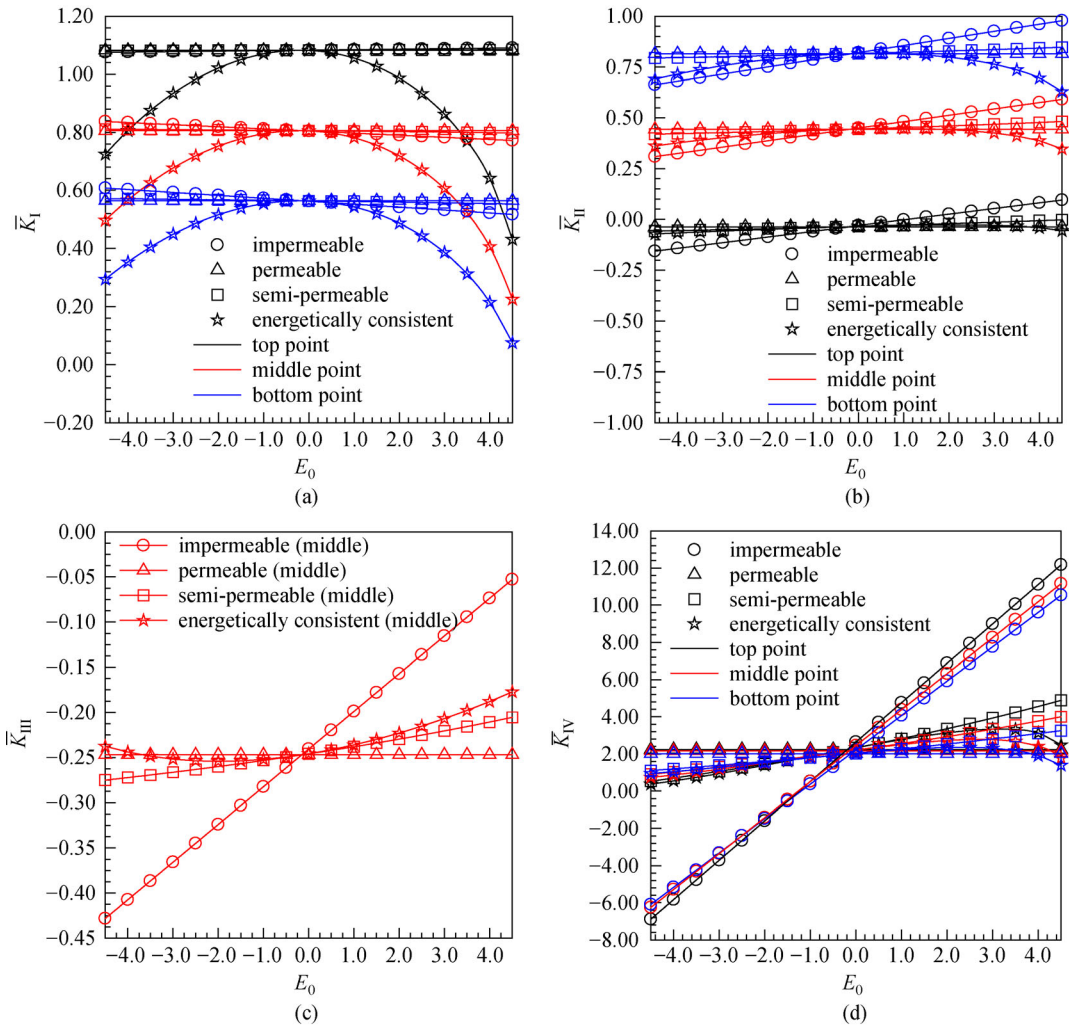

Fig. 9 Dependence of the normalized intensity factors on electric field for a cylindrical crack in a piezoelectric infinite medium: (a) $\overline{K}_{\mathrm{I}} = K_{\mathrm{I}}/(\sigma_0\sqrt{a})$; (b) $\overline{K}_{\mathrm{II}} = K_{\mathrm{II}}/(\sigma_0\sqrt{a})$; (c) $\overline{K}_{\mathrm{III}} = K_{\mathrm{III}}/(\sigma_0\sqrt{a})$; (d) $\overline{K}_{\mathrm{IV}} = (K_{\mathrm{IV}}E_{3333})/(\sigma_0 E_{3343}\sqrt{a})$.

$\{K_{\mathrm{I}},K_{\mathrm{II}},K_{\mathrm{III}},K_{\mathrm{IV}}\}$ at the top, middle, and bottom points of the cylindrical crack under the permeable crack-face condition are independent of the electric field. This similar conclusion was also observed for the case of a penny-shaped crack and a spherical cap crack.

5.4 Influence of permittivity of the medium inside the crack gap

To explore the influence of the permittivity of the medium inside the crack gap on the intensity factors along the crack front for both the spherical cap crack and the cylindrical crack (see Figs. 4 and 5) under semi-permeable and energetically consistent crack-face conditions, following parameters are used in the investigation: (i) the variation in the permittivity of the medium inside the crack gap, defined by $\kappa_{\mathrm{c}} = \alpha\kappa_0$ where α is the relative permittivity and $\kappa_0 = 8.85 \times 10^{-12}$ C/(Vm) is the permittivity of the air, is considered by varying α; (ii) the half-subtended angle is taken as $\theta = 45°$; (iii) the uniform remote tension and the uniform electric field are taken as 50 MPa and 2.5 MV/m, respectively; and (iv) the impermeable and permeable crack-face conditions are also considered in addition to the semi-permeable and energetically consistent cases to represent the cases $\alpha = 0$ and $\alpha = \infty$, respectively. Again, the meshes shown in Figs. 4(b) and 5(b) are employed in the analysis. Results for a penny-shaped crack of radius $a = R\theta$ are also obtained for the comparison purpose.

5.4.1 Spherical cap crack

The influence of the permittivity of the medium inside the spherical cap crack on the non-zero intensity factors, $\{K_{\mathrm{I}},K_{\mathrm{II}},K_{\mathrm{IV}}\}$ is demenstrated in Figs. 10(a)–10(c), respectively. It was observed that the mode-I stress intensity factors K_{I} of the penny-shaped crack under the semi-permeable crack-face condition is identical and clearly

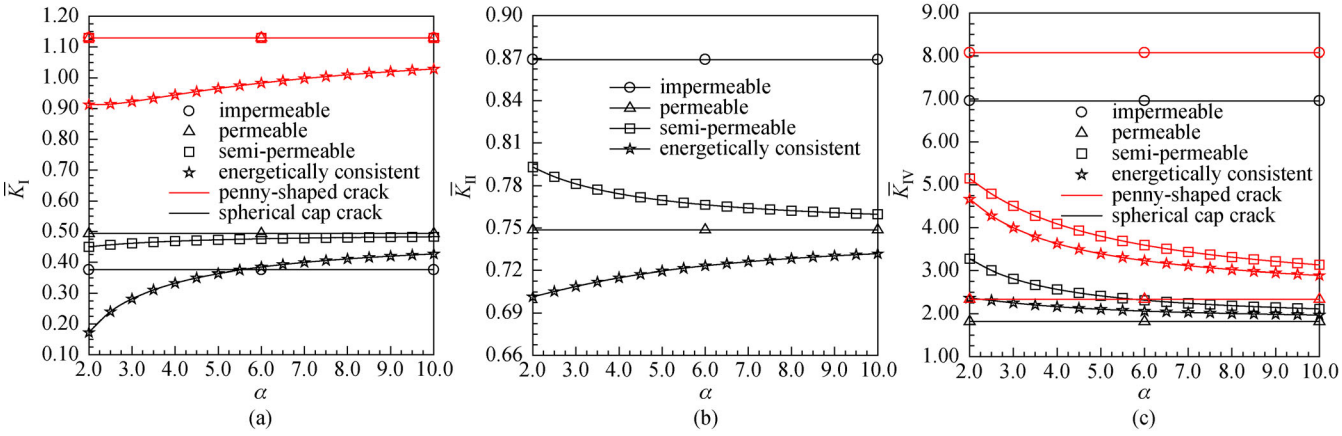

Fig. 10 Dependence of the normalized intensity factors on relative permittivity α of the medium inside the crack gap for a spherical cap crack in a piezoelectric infinite medium: (a) $\overline{K}_{\mathrm{I}} = K_{\mathrm{I}}/(\sigma_0\sqrt{a})$; (b) $\overline{K}_{\mathrm{II}} = K_{\mathrm{II}}/(\sigma_0\sqrt{a})$; (c) $\overline{K}_{\mathrm{IV}} = (K_{\mathrm{IV}}E_{3333})/(\sigma_0 E_{3343}\sqrt{a})$.

independent of the medium inside the crack gap and identical to those for the permeable and impermeable cases, while K_{I} of the same crack predicted by the energetically consistent model strongly depends on the medium inside the crack gap and it serves as the lower bound solution for the entire range of the relative permittivity α.

Unlike the penny-shaped crack, Fig. 10(a) shows that the results for the spherical cap crack obtained from the impermeable, permeable, and semi-permeable models are not identical and that the results for the semi-permeable crack depend on the medium inside the crack gap, whereas the results for the impermeable and permeable cases are completely different. Also, one can see that K_{I} for the semi-permeable crack varies from the impermeable solution to the permeable solution (which clearly represents the upper bound solution) as the value of the permittivity of the medium increases. This implies that the non-planar feature of the crack surface has the significant influence on the mode-I stress intensity factor of the three crack models. In addition, the numerical results also indicate that the lower bound of K_{I} for the special cap crack switches from the energetically consistent solution to the impermeable solution as the relative permittivity increases.

Figures 10(b) and 10(c) indicate that the mode-II stress intensity factor K_{II} and the electric intensity factor K_{IV} of the spherical cap crack under four crack-face conditions are significantly different according to the electrical boundary condition adopted on the crack surface. Moreover, it can be observed from obtained results that K_{II} and K_{IV} are strongly dependent on the permittivity of a medium inside the crack gap for both the semi-permeable and energetically consistent models. Such the results for both crack-face conditions approach the permeable solution as the permittivity of the medium increases. In addition, it can be seen that the impermeable solution represents the upper bound for both K_{II} and K_{IV} while the energetically consistent solution is the lower bound for the mode-II stress intensity factor K_{II} and the permeable solution serves as the lower bound for the electric intensity factor K_{IV}. Finally, it is important to note that the distribution of K_{IV} for the spherical cap crack under four crack-face conditions is similar to that of the penny-shaped crack.

5.4.2 Cylindrical crack

The normalized stress intensity factors K_{I}, K_{II}, K_{III}, and the electric intensity factor K_{IV} under four types of crack-face conditions are reported in Figs. 11(a)–11(d), respectively. Results in Fig. 11(a) indicate that the mode-I stress intensity factor K_{I} at the top point is greater than the middle and bottom points of the cylindrical crack. It can be also observed that K_{I} for the semi-permeable and energetically consistent models depends strongly on the permittivity of a medium inside the crack gap. In addition, the energetically consistent solution is significantly different from those of the other three crack-face models and it serves as the lower bound for the entire range of the relative permittivity α. This similar behavior is observed for the top, middle, and bottom points of the cylindrical crack. It is interesting to remark that the upper bounds of K_{I} at the three points of the cylindrical crack are not identical. More specifically, results at the top point for the impermeable, permeable, and semi-permeable crack-face conditions are nearly identical and serve as the upper bound, whereas the permeable solutions represent the upper bounds for both the middle and bottom points of the cylindrical crack.

Finally, it can be concluded that the lower and upper bounds of K_{I} for the penny-shaped crack, spherical cap crack, and cylindrical crack under four crack-face conditions are different. For the penny-shaped crack, the three crack-face models (i.e., impermeable, permeable, and semi-permeable models), and the energetically consistent crack-face model yield the upper and lower bound solutions, respectively, whereas, for the spherical cap

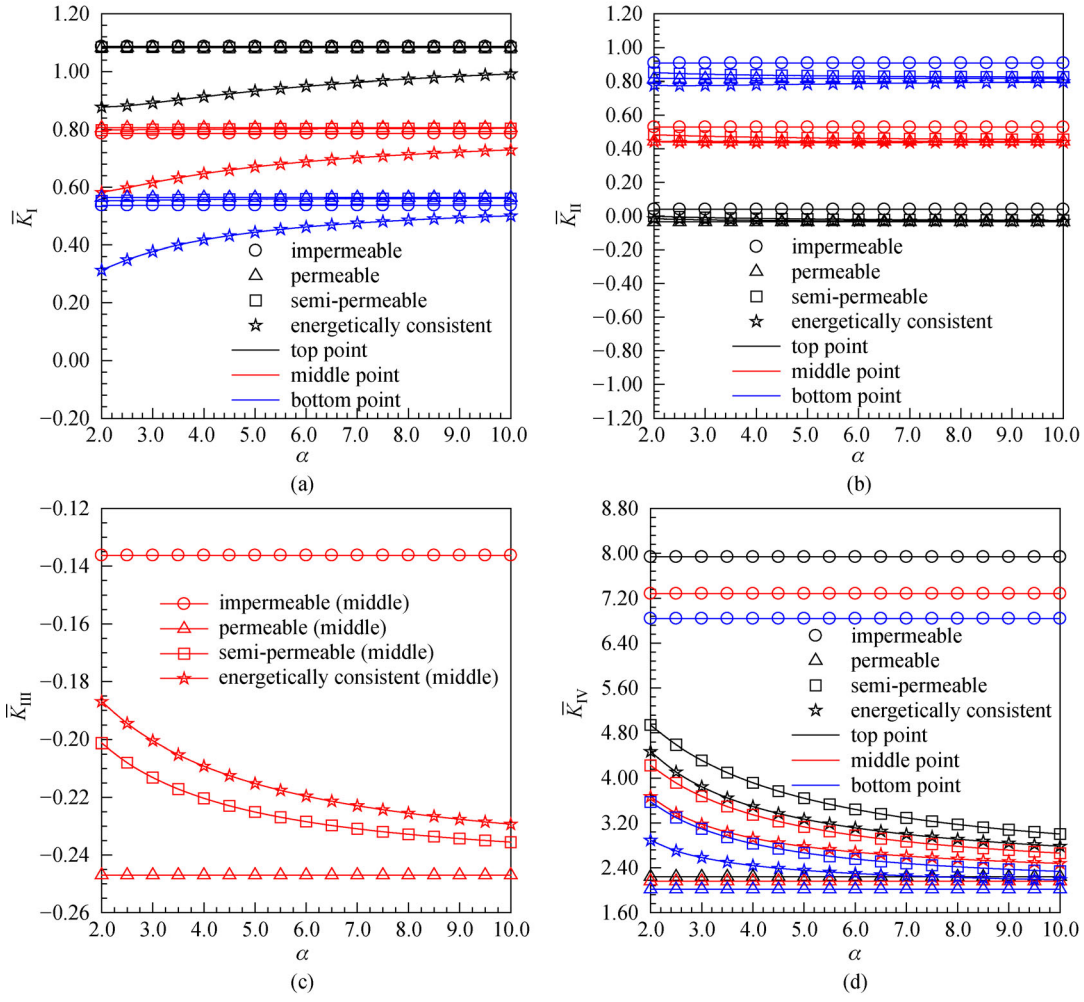

Fig. 11 Dependence of the normalized intensity factors on the relative permittivity α of the crack medium for a cylindrical crack in a piezoelectric infinite medium: (a) $\overline{K}_{\mathrm{I}} = K_{\mathrm{I}}/(\sigma_0\sqrt{a})$; (b) $\overline{K}_{\mathrm{II}} = K_{\mathrm{II}}/(\sigma_0\sqrt{a})$; (c) $\overline{K}_{\mathrm{III}} = K_{\mathrm{III}}/(\sigma_0\sqrt{a})$; (d) $\overline{K}_{\mathrm{IV}} = (K_{\mathrm{IV}}E_{3333})/(\sigma_0 E_{3343}\sqrt{a})$.

crack, the permeable solution serves as the upper bound while the lower bound switches from the energetically consistent solution to the impermeable solution as the permittivity of the medium inside the crack gap increases. However, for the cylindrical crack, the energetically consistent solution serves as the lower bound for all three points. One can also see that the semi-permeable solution is independent of the permittivity of the medium inside the crack gap for the penny-shaped crack but strongly depends on such quantity for both the spherical cap crack and the cylindrical crack.

Results in Fig. 11(b) indicate that the mode-II stress intensity factor K_{II} at the bottom point is greater than those at the middle and top points of the cylindrical crack. Similar to the mode-I stress intensity factor, K_{II} for the semi-permeable and energetically consistent condition is also strongly dependent on the permittivity of medium inside the crack gap. Results for both models vary from the impermeable solution to the permeable solution as the permittivity of the medium inside the crack gap increases. This finding is true for all three points of the cylindrical crack. In addition, one can observe that the impermeable solutions represent the upper bound for all three points of the cylindrical crack whereas the permeable solution serves as the lower bound for the top point and the energetically consistent solution represents the lower bound for the middle and bottom points for the cylindrical crack. This implies that the distribution of K_{II} for the middle and bottom points of the cylindrical crack is similar to that of the special cap crack. As a result, one can see that the upper and lower bounds of the middle and bottom points of the cylindrical crack are the same as those for the spherical cap crack.

From results of the non-zero mode-III stress intensity factor K_{III} at the middle point of the cylindrical crack shown in Fig. 11(c), the semi-permeable and energetically consistent solutions, again, depend strongly on the permittivity of the medium inside the crack gap and both results varies from the impermeable solution to the permeable solution as the permittivity of the medium

increases. Clearly, the impermeable solution serves as the upper bound whereas the permeable solution represents the lower bound for the entire range of the relative permittivity α.

Results reported in Fig. 11(d) indicate that the electric intensity factor K_{IV} at the top point is greater than those at the middle and bottom points of the cylindrical crack. Moreover, it was found that the behavior of K_{IV} at the three points of the cylindrical crack is similar to that of the penny-shaped crack and the spherical cap crack. More specifically, K_{IV} generated from the semi-permeable and energetically consistent models strongly depends on the relative permittivity α of the medium inside the crack gap and both results vary from the impermeable solution that is the upper bound to the permeable solution that is the lower bound as α increases.

6 Conclusions

In the present study, we have fully investigated the influence of half subtended angle on the intensity factors of three crack configurations including the penny-shaped crack, the spherical cap crack, and the cylindrical crack under impermeable, permeable, semi-permeable, and energetically consistent crack-face conditions. Obtained results have indicated that the mode-I stress intensity factor K_I and the electric intensity factor K_{IV} at the top and bottom points of the cylindrical crack have the similar behavior to that of the penny-shaped crack and the spherical cap crack, respectively, whereas $\{K_I,K_{IV}\}$ at the middle point of the cylindrical crack have different trend when compared with those for the penny-shaped crack and the spherical cap crack. However, for the relatively small half-subtended angle (e.g., $\theta = 5°,10°$), the characteristics of $\{K_I,K_{IV}\}$ for the spherical cap crack and the cylindrical crack are similar to those for the penny-shaped crack.

For the penny-shaped crack subjected to a uniform loading, the mode-II and mode-III stress intensity factors vanish identically for all four types of crack-face conditions considered due to the symmetry. In contrast, due to the non-flat feature of the crack surface, the mode-II stress intensity factor of the spherical cap crack and the cylindrical crack and the mode-III stress intensity factor of the cylindrical crack do not vanish along the crack front. It was also found that when the half-subtended angle of the spherical cap crack and the cylindrical crack are sufficiently large, the non-zero mode-II and mode-III stress intensity factors under the four crack-face conditions are different according to the electrical boundary condition adopted on the crack surface. As a result, the upper and lower bounds of the mode-II and mode-III stress intensity factors could be seen. In particular, the impermeable solution represents the upper bound of the mode-II stress intensity factor of the spherical cap crack and the three representative points for the cylindrical crack, and as well as the upper bound of the mode-III stress intensity factor at the middle point of the cylindrical crack. However, the energetically consistent solution represents the lower bound of the mode-II stress intensity factor of the spherical cap crack and the middle and bottom points of the cylindrical crack, whereas the permeable solution serves as the lower bound of the mode-II and mode-III stress intensity factors at the top and middle points of the cylindrical crack, respectively.

Results from the investigation of the influence of the electric field on the intensity factors for the three representative crack configurations under four different crack-face conditions have indicated that the non-zero intensity factors $\{K_I,K_{II},K_{III},K_{IV}\}$ under the permeable and energetically consistent crack-face conditions for both planar (i.e., penny-shaped crack) and non-planar cracks (i.e., spherical cap and cylindrical cracks) were independent and dependent of the electric field, respectively. In addition, it was found that the influence of the electric field on the electric intensity factor K_{IV} for the penny-shaped crack was similar to that for the spherical cap crack and cylindrical crack under the four crack-face conditions. In particular, K_{IV} obtained from the impermeable, semi-permeable, and energetically consistent models depends strongly on the electric field, whereas K_{IV} of the permeable crack is independent of the electric filed. On the contrary, the behavior of the mode-I stress intensity factor K_I under the impermeable and semi-permeable conditions for the planar crack (i.e., penny-shaped) and the non-planar cracks (i.e., spherical cap crack, and the middle and bottom points of the cylindrical crack) are different. In particular, K_I of the impermeable and semi-permeable spherical cap crack depends strongly on the electric field whereas such results for the penny-shaped crack are independent of the electric field. This implies that the non-flat crack surface renders the dependence on the electric field for K_I for both the impermeable and semi-permeable crack-face conditions.

Finally, it can be concluded that all the intensity factors $\{K_I,K_{II},K_{III},K_{IV}\}$ for the three representative crack configurations under the energetically consistent crack-face condition strongly depend on the permittivity of the medium inside the crack gap. The same behavior can also be observed for the semi-permeable crack-face condition, except for the mode-I stress intensity factor K_I of the penny-shaped crack that is found independent of the medium inside the crack gap.

Acknowledgements The authors gratefully acknowledge the financial support provided by Thailand Research Fund (Grant Nos. TRG5880100 and RSA5980032).

References

1. Kuna M. Fracture mechanics of piezoelectric materials—where are we right now? Engineering Fracture Mechanics, 2010, 77(2): 309–

326
2. Sladek J, Sladek V, Wünsche M, Zhang C. Effects of electric field and strain gradients on cracks in piezoelectric solids. European Journal of Mechanics. A, Solids, 2018, 71: 187–198
3. Sladek J, Sladek V, Stanak P, Zhang C, Tan C L. Fracture mechanics analysis of size-dependent piezoelectric solids. International Journal of Solids and Structures, 2017, 113–114: 1–9
4. Ghasemi H, Park H S, Rabczuk T. A multi-material level set-based topology optimization of flexoelectric composites. Computer Methods in Applied Mechanics and Engineering, 2018, 332: 47–62
5. Hamdia K M, Ghasemi H, Zhuang X, Alajlan N, Rabczuk T. Sensitivity and uncertainly analysis for flexoelectric nanostructures. Computer Methods in Applied Mechanics and Engineering, 2018, 337: 95–109
6. Thai T Q, Rabczuk T, Zhuang X. A large deformation isogeometric approach for flexoelectricity and soft materials. Computer Methods in Applied Mechanics and Engineering, 2018, 341: 718–739
7. Nguyen B H, Nanthakumar S S, Zhuang X, Wriggers P, Jiang X, Rabczuk T. Dynamic flexoelectric effect on piezoelectric nanostructures. European Journal of Mechanics. A, Solids, 2018, 71: 404–409
8. Ghasemi H, Park H S, Rabczuk T. A level-set based IGA formulation for topology optimization of flexoelectric materials. Computer Methods in Applied Mechanics and Engineering, 2017, 313: 239–258
9. Nanthakumar S S, Lahmer T, Zhuang X, Zi G, Rabczuk T. Detection of material interfaces using a regularized level set method in piezoelectric structures. Inverse Problems in Science and Engineering, 2016, 24(1): 153–176
10. Mishra R K. A review on fracture mechanics in piezoelectric structures. In: Proceedings of Materials Today. Amsterdam: Elsevier, 2018, 5407–5413
11. Parton V Z. Fracture mechanics of piezoelectric materials. Acta Astronautica, 1976, 3(9–10): 671–683
12. Deeg W F. The analysis of dislocation, crack and inclusion problems in piezoelectric solids. Dissertation for the Doctoral Degree. Palo Alto: Standford University, 1980
13. Hao T H, Shen Z Y. A new electric boundary condition of electric fracture mechanics and its applications. Engineering Fracture Mechanics, 1994, 47(6): 793–802
14. Landis C M. Energetically consistent boundary conditions for electromechanical fracture. International Journal of Solids and Structures, 2004, 41(22–23): 6291–6315
15. Rungamornrat J, Phongtinnaboot W, Wijeyewickrema A C. Analysis of cracks in 3D piezoelectric media with various electrical boundary conditions. International Journal of Fracture, 2015, 192(2): 133–153
16. Park S B, Sun C T. Effect of electric field on fracture of piezoelectric ceramics. International Journal of Fracture, 1993, 70(3): 203–216
17. Pan E. A BEM analysis of fracture mechanics in 2D anisotropic piezoelectric solids. Engineering Analysis with Boundary Elements, 1999, 23(1): 67–76
18. Chen W Q, Shioya T. Fundamental solution for a penny-shaped crack in a piezoelectric medium. Journal of the Mechanics and Physics of Solids, 1999, 47(7): 1459–1475
19. Chen W Q, Shioya T. Complete and exact solutions of a penny-shaped crack in a piezoelectric solid: Antisymmetric shear loadings. International Journal of Solids and Structures, 2000, 37(18): 2603–2619
20. Chen W Q, Shioya T, Ding H J. A penny-shaped crack in piezoelectrics: Resolved. International Journal of Fracture, 2000, 105(1): 49–56
21. Xu X L, Rajapakse R K N D. A theoretical study of branched cracks in piezoelectrics. Acta Materialia, 2000, 48(8): 1865–1882
22. Davì G, Milazzo A. Multidomain boundary integral formulation for piezoelectric materials fracture mechanics. International Journal of Solids and Structures, 2001, 38(40–41): 7065–7078
23. Hou P F, Ding H J, Guan F L. Point forces and point charge applied to a circular crack in a transversely isotropic piezoelectric space. Theoretical and Applied Fracture Mechanics, 2001, 36(3): 245–262
24. Rajapakse R K N D, Xu X L. Boundary element modeling of cracks in piezoelectric solids. Engineering Analysis with Boundary Elements, 2001, 25(9): 771–781
25. Xu X L, Rajapakse R K N D. On a plane crack in piezoelectric solids. International Journal of Solids and Structures, 2001, 38(42–43): 7643–7658
26. Wang X D, Jiang L Y. Fracture behaviour of cracks in piezoelectric media with electromechanically coupled boundary conditions. Proceeding of the Royal Society A: Mathematical, Physical and Engineering Sciences, 2002, 458(2026): 2545–2560
27. Huang Z, Kuang Z B. A mixed electric boundary value problem for a two-dimensional piezoelectric crack. International Journal of Solids and Structures, 2003, 40(6): 1433–1453
28. Wang B L, Mai Y W. On the electrical boundary conditions on the crack surfaces in piezoelectric ceramics. International Journal of Engineering Science, 2003, 41(6): 633–652
29. Chen M C. Application of finite-part integrals to three-dimensional fracture problems for piezoelectric media Part I: Hypersingular integral equation and theoretical analysis. International Journal of Fracture, 2003, 121(3–4): 133–148
30. Chen M C. Application of finite-part integrals to three-dimensional fracture problems for piezoelectric media Part II: Numerical analysis. International Journal of Fracture, 2003, 121(3–4): 149–161
31. Wang X D, Jiang L Y. The nonlinear fracture behaviour of an arbitrarily oriented dielectric crack in piezoelectric materials. Acta Mechanica, 2004, 172(3–4): 195–210
32. Li X F, Lee K Y. Three-dimensional electroelastic analysis of a piezoelectric material with a penny-shaped dielectric crack. ASME Journal of Applied Mechanics, 2004, 71(6): 866–878
33. Chen W Q, Lim C W. 3D point force solution for a permeable penny-shaped crack embedded in an infinite transversely isotropic piezoelectric medium. International Journal of Fracture, 2005, 131(3): 231–246
34. Groh U, Kuna M. Efficient boundary element analysis of cracks in 2D piezoelectric structures. International Journal of Solids and Structures, 2005, 42(8): 2399–2416
35. Chiang C R, Weng G J. Nonlinear behavior and critical state of a penny-shaped dielectric crack in a piezoelectric solid. ASME Journal of Applied Mechanics, 2007, 74(5): 852–860
36. Ou Z C, Chen Y H. Re-examination of the PKHS crack model in piezoelectric materials. European Journal of Mechanics. A, Solids, 2007, 26(4): 659–675

37. Qin T Y, Yu Y S, Noda N A. Finite-part integral and boundary element method to solve three-dimensional crack problems in piezoelectric materials. International Journal of Solids and Structures, 2007, 44(14–15): 4770–4783
38. Wippler K, Kuna M. Crack analyses in three-dimensional piezoelectric structures by the BEM. Computational Materials Science, 2007, 39(1): 261–266
39. Li Q, Ricoeur A, Kuna M. Coulomb traction on a penny-shaped crack in a three-dimensional piezoelectric body. Archive of Applied Mechanics, 2011, 81(6): 685–700
40. Lei J, Wang H, Zhang C, Bui T, Garcia-Sanchez F. Comparison of several BEM-based approaches in evaluating crack-tip field intensity factors in piezoelectric materials. International Journal of Fracture, 2014, 189(1): 111–120
41. Lei J, Zhang C, Garcia-Sanchez F. BEM analysis of electrically limited permeable cracks considering Coulomb tractions in piezoelectric materials. Engineering Analysis with Boundary Elements, 2015, 54: 28–38
42. Lei J, Yun L, Zhang C. An interaction integral and a modified crack closure integral for evaluating piezoelectric crack-tip fracture parameters in BEM. Engineering Analysis with Boundary Elements, 2017, 79: 88–97
43. Lei J, Zhang C. A simplified evaluation of the mechanical energy release rate of kinked cracks in piezoelectric materials using the boundary element method. Engineering Fracture Mechanics, 2018, 188: 36–57
44. Xu C H, Zhou Z H, Leung A Y T, Xu X S, Luo X W. The finite element discretized symplectic method for direct computation of SIF of piezoelectric materials. Engineering Fracture Mechanics, 2016, 162: 21–37
45. Hao T. Multiple collinear cracks in a piezoelectric material. International Journal of Solids and Structures, 2001, 38(50–51): 9201–9208
46. Denda M, Mansukh M. Upper and lower bounds analysis of electric induction intensity factors for multiple piezoelectric cracks by the BEM. Engineering Analysis with Boundary Elements, 2005, 29(6): 533–550
47. Sanz J A, Ariza M P, Dominguez J. Three-dimensional BEM for piezoelectric fracture analysis. Engineering Analysis with Boundary Elements, 2005, 29(6): 586–596
48. Rungamornrat J, Mear M E. Analysis of fractures in 3D piezoelectric media by a weakly singular integral equation method. International Journal of Fracture, 2008, 151(1): 1–27
49. Solis M, Sanz J A, Ariza M P, Dominguez J. Analysis of cracked piezoelectric solids by a mixed three-dimensional BE approach. Engineering Analysis with Boundary Elements, 2009, 33(3): 271–282
50. Li Q, Chen Y H. Why traction-free? Piezoelectric crack and coulombic traction. Archive of Applied Mechanics, 2008, 78(7): 559–573
51. Motola Y, Banks-Sills L. M-integral for calculating intensity factors of cracked piezoelectric materials using the exact boundary conditions. ASME Journal of Applied Mechanics, 2008, 76(1): 011004
52. Phongtinnaboot W, Rungamornrat J, Chintanapakdee C. Modeling of cracks in 3D piezoelectric finite media by weakly singular SGBEM. Engineering Analysis with Boundary Elements, 2011, 35(3): 319–329
53. Martin P A, Rizzo F J. Hypersingular integrals: How smooth must the density be? International Journal for Numerical Methods in Engineering, 1996, 39(4): 687–704
54. Pan E. A BEM analysis of fracture mechanics in 2D anisotropic piezoelectric solids. Engineering Analysis with Boundary Elements, 1999, 23(1): 67–76
55. Chen M C. Application of finite-part integrals to three-dimensional fracture problems for piezoelectric media Part I: Hypersingular integral equation and theoretical analysis. International Journal of Fracture, 2003, 121(3–4): 133–148
56. Chen M C. Application of finite-part integrals to three-dimensional fracture problems for piezoelectric media Part II: numerical analysis. International Journal of Fracture, 2003, 121(3–4): 149–161
57. Qin T Y, Noda N A. Application of hypersingular integral equation method to a three-dimensional crack in piezoelectric materials. JSME International Journal. Series A, Solid Mechanics and Material Engineering, 2004, 47(2): 173–180
58. Li S, Mear M E, Xiao L. Symmetric weak-form integral equation method for three-dimensional fracture analysis. Computer Methods in Applied Mechanics and Engineering, 1998, 151(3–4): 435–459